Influence of supplementary cementitious materials on microstructure and transport properties of spacer-concrete interface

F. Muslim[1, 2], H.S. Wong[1*], T.H. Choo[1] and N.R. Buenfeld[1]

[1]*Centre for Infrastructure Materials, Imperial College London, SW7 2AZ, UK*

[2]*Civil Engineering Department, Faculty of Engineering, Universitas Indonesia, Kampus UI, Depok 16424, Indonesia*

Abstract

Reinforcement spacers are a critical component of concrete structures. Their presence affects microstructure and transport properties of concrete cover though this is not widely appreciated. This paper presents the first study to determine whether the negative effects of spacers can be mitigated through the use of supplementary cementitious materials such as silica fume, fly ash and blast-furnace slag. Concrete samples (>200) with different spacers, binders, curing and drying regimes were prepared and tested for diffusion, permeation, absorption, electrical conductivity, carbonation and microstructure. It was found that spacers increase all transport properties, the extent depending on type of spacer, drying regime and transport mechanism. The spacer-concrete interface is weak, porous and micro-cracked, and this lowers the resistance of concrete to ingress of aggressive agents. The beneficial effects of SCMs (strength enhancement and densification) and prolonged curing (120-day) are insufficient to overcome the negative effects of spacers. Implications for durability are discussed.

Keywords: Interfacial transition zone (B); Microstructure (B); Durability (C); Transport properties (C); Blended cement (D); Spacers

1. Introduction

Reinforcement spacers are devices used in conventional reinforced concrete to support reinforcing steel in the formwork so that the required nominal cover is achieved for durability and fire protection. Spacers come in a wide range of shapes and sizes, and are made from either plastic, cementitious material or steel wire [1-5]. They are also known as bar supports, chairs, bolsters etc., but the general term “spacers” will be used in this paper. The most popular spacer types are made from plastic because they are low cost and do not require labour intensive operation of securing the reinforcement with tying wire. Design codes of practice for concrete structures require a spacer to be located at every meter (or less) to ensure that the steel reinforcements remain in place during concreting, and the spacers are then left permanently in the structure [6-10]. Therefore, a typical concrete element will contain many spacers.

Because spacers function by holding the rebar from the formwork, they inevitably form an interface between the reinforcing steel and cast surface through the concrete cover. As such, it is possible that spacers compromise the integrity of the concrete cover and its effectiveness to protect embedded reinforcement. Spacers may act as weak links that facilitate ingress of aggressive agents causing premature deterioration. Indeed, some field investigations have reported correlation between the location of spacers and reinforcement corrosion [11-16]. Yet surprisingly very little fundamental research has been carried out on the influence of spacers on the long-term durability of concrete structures.

Alzyoud et al. [17] reported the first systematic study to understand how reinforcement spacers influence the microstructure and mass transport properties of concrete. Samples with a range of spacer types, cover depths, curing ages and conditioning (drying) regimes were tested for oxygen diffusion, oxygen permeation, water absorption, chloride penetration and microstructure. They found that spacers increased mass transport in all cases. This was attributed to preferential flow via the interface between spacer and concrete that was shown to be highly porous and micro-cracked. However, a major limitation of the study is that it was based entirely on concretes made from ordinary Portland cement (CEM I) only. Modern concretes frequently contain

* Corresponding author. Tel: +44 (0)20 7594 5956.
E-mail: hong.wong@imperial.ac.uk

supplementary cementitious materials (SCMs) as partial replacement for CEM I and the study by Alzyoud et al. [17] did not include such systems.

The most common SCMs are industrial by-products such as pulverised fuel ash or fly ash (FA), ground granulated blastfurnace slag (GGBS) and silica fume (SF). These have been widely studied and used for many decades, initially to reduce cost, but now as a means to improve engineering properties, long-term durability and sustainability of concrete [18]. It is well-known that blending CEM I with reactive SCMs is effective in densifying the microstructure and reducing ingress of aggressive species [19-22]. SCMs are pozzolanic and some may display hydraulic reactivity (e.g. GGBS). Silica fume is a particularly reactive pozzolan that also acts as a micro-filler and provides additional nucleation sites to accelerate cement hydration. SCMs may improve particle packing and generate additional hydration products that refine the overall microstructure of concrete, in particular the interface between aggregate and cement paste (ITZ) [23-25]. Therefore, it is reasonable to expect that the same improvements should occur at the spacer-concrete interface, however this has not been established.

The aim of this study is to characterise the properties of the spacer-concrete interface containing SCMs such as FA, GGBS and SF. The main questions that this study wishes to answer are: a) What is the influence of SCMs on the microstructure and mass transport properties of the spacer-concrete interface? b) How do these blended systems compare against pure CEM I systems? and c) Can the beneficial properties of SCMs mitigate the negative effects of reinforcement spacers?

2. Experimental

2.1 Materials and mix proportions

Cementitious spacers (CS) and plastic 'A' spacers (PS) for 50 mm cover, as shown in Fig. 1 were used. These were produced by a major spacers manufacturer and are widely used in the UK and elsewhere. The cementitious spacer was a Portland cement mortar with 50% GGBS at water/binder ratio (w/b) 0.35 that was reinforced with polypropylene fibres. It had a water assessible porosity of 8.5% determined by vacuum saturation from 60 ± 5% RH, 21ºC and water sorptivity of 35 $g/m^2.mm^{0.5}$. The plastic spacer was made of polyvinyl chloride (PVC). The total surface areas of CS and PS were 1860 mm^2 and 2560 mm^2 respectively. The spacers were stored in a laboratory environment (60 ± 5% RH, 21ºC) to avoid moisture or temperature variations prior to casting in concrete.

Three blended concrete mixes were prepared using Portland cement CEM I 52.5N and cement replacement by 8% silica fume (SF), 30% fly ash (FA), or 60% ground granulated blast-furnace slag (GGBS) at free w/b ratio of 0.4. The cements conformed to BS EN 197-1:2011 [26], BS EN 13263-1:2005 [27], BS EN 450-1:2012 [28] and BS EN 15167-1:2006 [29] respectively. The composition and properties of the cements are given in Table 1.

Concrete mix proportions are shown in Table 2. These were designed to absolute volume [30] with total aggregate content of 70% vol. and sand-to-total aggregate mass ratio of 0.4. Thames Valley gravel (< 10 mm) and sand (< 5 mm) complying with BS EN 12620:2002 [31] were used. The specific gravity of the coarse and fine aggregates were 2.75 and 2.51 respectively. The 24-h water absorption to saturated surface dry condition of the combined aggregate was 0.6%. A superplasticiser (Sika ViscoCrete 20RM) was used at 0.5% wt. of binder to improve workability. Tap water was used for batching. The volume of water was corrected for the amount absorbed by the aggregate particles and to exclude water from the superplasticizer.

2.2 Sample preparation, curing and conditioning

A total of 216 cylindrical samples (100∅ × 50 mm) were prepared. Details are summarised in Table 3. Samples were cast in steel moulds shown in Fig. 2. A spacer was secured in the centre of each mould using high-yield reinforcing steel (12∅ mm) and timber beams attached to the base plate prior to concreting. This was to ensure that the spacer and rebar did not move during concrete placement and compaction, which would otherwise influence results. The smallest clearance available in the mould for placing concrete was at least 3.5× the maximum aggregate size near the top and 2.5× maximum aggregate size at the bottom. These satisfy clear spacing requirements to allow concrete placement and compaction [32]. Visual checks found that the mould assembly worked well and there was no displacement of the spacer and rebar, or aggregate

segregation during concreting. The volume fraction occupied by the cementitious spacer was ~14% and ~ 7% for the plastic spacer.

Mix ingredients were batched by weight. Solids were first dry mixed for 30s in a 30-liter pan mixer. Batch water pre-mixed with superplasticiser was then added and mixing was continued for another 3 min. The mixes had slump between 90 and 100 mm. Samples were compacted with a vibrating table in two equal layers until no significant air bubbles escaped. The fresh samples were covered with plastic sheeting and wet hessian, and kept at room temperature for the first 24 h prior to demoulding. The density of the hardened concrete was measured after demoulding in accordance with BS EN 12390-7:2009 [33]. This was compared with the theoretical density obtained from the mix proportions and density of the spacer, to ensure that good compaction was achieved without excessive voidage.

Curing was carried out by either sealing in cling film and polyethylene bags for 3 days at 21°C to simulate on-site curing (using impervious sheeting or membrane), or in a fog room at 21°C, 100% RH for 28 and 120 days to produce well-hydrated samples. Samples were then dried (conditioned) at 21°C, 75 ± 1% RH to constant mass so that the transport results were not affected by changes in moisture. This regime was chosen to represent gentle drying and to minimize shrinkage-induced microcracking [34]. The conditioning boxes contained saturated NaCl to maintain 75% RH, soda lime to prevent carbonation, and fans to circulate air. RH was monitored and the salt solution replaced when necessary. Drying to constant mass (< 0.01% mass loss per day) required ~3 to 4 months. Replicate samples were dried at 50°C, 7% RH to simulate severe drying in hot weather. Samples were then cooled in a vacuum desiccator at 21°C to avoid condensation. The moisture content after conditioning at 21°C, 75 ± 1% RH and 50°C, 7% RH ranged from 2.5 to 5% and 0.5 to 1% respectively.

2.3 Oxygen diffusion, oxygen permeation, water absorption and electrical conductivity

Three replicate samples were tested following the sequence of oxygen diffusivity, oxygen permeability, water sorptivity and electrical conductivity. Diffusivity and permeability were carried out by placing the sample in a steel cell that was sealed with silicone rubber ring and confined by a small pressure of 0.57 MPa. This ensured that gas flow occurred via the sample only without leaking through side or causing further cracking or closure of existing cracks [35].

Oxygen diffusion was carried out by exposing opposite faces of the sample to oxygen and nitrogen at equal temperature and pressure. The flow rates were allowed to stabilise and a zirconia oxygen analyser was then used to measure the concentration of oxygen in the outflow stream [36]. A similar assembly was used to measure oxygen permeability at ~0.05, 0.15 and 0.25 MPa gas pressures. The outflow rate at each pressure was measured at steady state using flowmeters. Darcy's equation for incompressible fluids was used to calculate apparent permeability at the applied pressure and Klinkenberg's method was used to correct for gas slippage to obtain intrinsic permeability [37].

Water absorption was conducted using the conventional gravimetric capillary rise method. The sample was placed on plastic strips in a tray containing shallow water (~3 mm), and the mass gain with time until saturation was measured using a balance accurate to 0.01 g. A loose fitting transparent lid was used to cover the tray to prevent the sample from drying and to avoid condensation. The sorptivity coefficient was calculated from the slope of the best-fit line of the cumulative absorption vs. square-root time plot. This was fitted across 10 readings or more from the first 7 hours of absorption. The coefficient of determination (R^2) was greater than 0.95 in all cases.

Samples were vacuum saturated in water for ~ 4 h and left immersed for 24 h to determine accessible porosity from the pre-conditioned state. Electrical conductivity was then carried out on the saturated-surface dry samples in between two brass electrodes. Salt-free electrode gel was applied to ensure good contact. An LCR databridge was used to measure the A.C. electrical resistance at 1 kHz frequency to reduce polarisation effects. Electrical conductivity was calculated from the electrical resistance and sample dimensions.

2.4 Epoxy impregnation

Replicate samples were prepared and conditioned as described in Section 2.2, and then pressure impregnated with low viscosity fluorescein dyed epoxy resin, following the procedures described by Wu et al. [38, 39]. This was carried out in a pressure cell shown in Fig. 3a that is similar to the one used for gas permeability testing. The sample surface was covered with fluorescein dyed epoxy (Struers EpoFix resin with EpoDye, 5% toluene dilution) and 10 bar compressed air was applied overnight to impregnate the sample. After two

days of curing at room temperature, the impregnated samples were cut in half with a diamond abrasive cutter and ground with silicon carbide at 120-grit. Fluorescent images were captured in a dark room using a single-lens reflex digital camera. To induce uniform fluorescence, the sample was illuminated with 15 W 50 Hz UV lamp placed at a fixed distance of 50 mm above (Fig. 3b). The whole surface (~100 × 50 mm) was imaged at 2450 × 1255 pixels. The camera was set at low ISO (200) to reduce noise, small aperture (f/22) to increase depth of field and slow shutter speed (8 s) to achieve good exposure. Images were then analysed to determine the penetration and spatial distribution of the intruded epoxy.

2.5 Carbonation depth

Two replicate samples were cured in a fog room for 120 days, then conditioned at 21°C and 75% RH until constant mass. To ensure unidirectional transport, several layers of waterproof tape were applied on all sides except the flat cast surface (where the spacer base is located). The samples were then exposed to accelerated carbonation at 3% CO_2, 30°C and 75% RH for 7 months. Following that, the carbonated samples were cut in half with diamond abrasive cutter and sandblasted to expose a fresh surface. This was then cleaned with compressed air to remove dust and sprayed with 1% phenolphthalein solution [40]. Within 30 s of applying phenolphthalein, the entire cross section was scanned with a digital stereo microscope (Olympus SZX9). The carbonation depth was measured on at least 10 locations using image analysis.

2.6 Microstructure of spacer-concrete interface

Microstructure of the interface between spacer and concrete was characterised using Euclidean distance mapping (EDM) [41]. Samples were dried at 40°C and epoxy-impregnated to preserve the spacer-concrete interface. A block (~40 × 20 × 8 mm) spanning the interface was extracted, vacuum impregnated with low viscosity fluorescein epoxy and then subjected to additional 0.25 MPa pressure for 2 h to achieve complete impregnation. Surface grinding was then carried out with SiC at grit sizes of 68 µm, 30 µm, 18 µm and 14 µm. Finally, the blocks were diamond polished at 9 µm, 6 µm, 3 µm, 1 µm and 0.25 µm with non-aqueous lubricant to achieve a flat surface for high resolution imaging. Polished blocks were cleaned with acetone and kept in a desiccator.

Fifty images of the interface were collected per sample using laser scanning confocal microscopy (LSCM) and backscattered electron (BSE) microscopy. LSCM was carried out on a Leica TCS SP5 microscope with 40× oil immersion objective at 1.25 numerical aperture. The sample was illuminated with 488 nm argon laser at 15% intensity to match the maximum absorption wavelength of fluorescein dye to ensure optimal fluorescence [42, 43]. Fluorescence emissions at 500-600 nm were filtered and collected with the PMT detector. Pinhole size was fixed at 1 Airy unit and two-times line averaging was applied to reduce noise. Images were digitised to 2048 × 2048 pixels at 0.189 µm spacing. BSE imaging was carried out using Hitachi TM4000 SEM operated at 10 keV beam energy and 1 cm working distance. Samples were carbon coated to avoid charging effects. BSE images (2560 × 1920 pixels) were obtained at 500x magnification and 0.099 µm pixel size.

Imaging was carried out at ~ 1 mm interval along the interface to attain random unbiased sampling. Care was taken to avoid aggregate particles located close to the spacer (< 50 µm) so that the analysis is not affected by the aggregate-paste ITZ. Brightness and contrast settings were calibrated to utilise the full range of the brightness histogram. Finally, image analysis was carried out with FIJI/Image J [44, 45] to measure spatial distributions of porosity and anhydrous cement from the interface at one-pixel strip width [41]. Segmentation of pores and microcracks was carried out using the moment-preserving method [46] for LSCM and overflow method [47] for BSE images.

3. Results

3.1 Transport properties after drying

Table 4 presents the oxygen diffusivity, oxygen permeability and water sorptivity measured after conditioning at 21ºC, 75% RH. For diffusivity and sorptivity, the highest results were over 20 times the lowest, ranging from 2.4×10^{-9} to 50.6×10^{-9} m^2/s and 6.5 to 155.8 $g/m^2min^{0.5}$ respectively. In contrast, oxygen permeability spanned over three decades from 1.1×10^{-18} to 4.2×10^{-15} m^2. As expected, transport decreased with increasing curing age. Samples containing SF gave the lowest transport properties, followed by GGBS

and FA. However, it is worth noting that the changes induced by curing age or binder type in the vast majority of cases were less than a factor 2.

Samples dried at 50ºC consistently produced much higher transport coefficients (Table 5) compared to those dried at 21ºC, 75% RH. The difference was up by a factor of 18 for sorptivity, 21 for diffusivity and 643 for permeability. Therefore, the change in transport caused by drying is much larger compared to increasing curing age (3 to 120 days) or varying binder type (SF, FA, GGBS). Permeability is much more sensitive to drying compared to diffusivity or sorptivity, which is expected and consistent with previous studies [38, 39, 48]. In addition, concretes that are mature (longer curing ages) and denser (e.g. containing SF) experienced a greater increase in transport on drying. For example, Fig. 4 shows an inverse relationship between the percentage increase in transport after drying at 50ºC, 7% RH and 21ºC, 75% RH. The effect of damage caused by drying is more severe on denser samples, which agrees with numerical simulations [49].

It is also worth noting that during capillary absorption (sorptivity testing), the 50°C dried samples showed a slight non-linear behaviour between cumulative absorption and square-root of time, where the initial mass gain was followed by a more rapid mass gain before stabilising to indicate saturation. This sigmoidal or *S*-shaped behavior was not observed in gently dried samples at 21°C, 75% RH. This anomalous absorption is caused by drying-induced microcracking [34, 36].

3.2 Effect of spacers on mass transport

The data presented in Table 4 and Table 5 show that spacers increase mass transport. To illustrate this further, transport properties of samples containing spacers are normalised to their respective control references without spacer, and the data are plotted in Fig. 5. The normalised data for 100% CEM I systems from Alzyoud et al. [17] for the same spacer types, curing and conditioning regimes are included as comparison to the blended systems tested in this study.

The normalised transport values range from 0.7 to 57. Out of 120 pairs of data, 104 sets (87%) show normalised transport > 1. Therefore, samples that contained spacers had higher transport properties compared to their respective control reference in the vast majority of the cases. The average normalised value is ~1.4 for diffusivity and sorptivity, and ~12 for permeability. This shows that the permeability is significantly more affected by spacers. Samples with plastic spacers performed significantly worse, increasing transport by up to a factor of 57×, compared to 16× for cementitious spacers.

The normalised data do not show a consistent trend with curing age or binder type. Samples that were cured longer or those containing SCMs do not show much reduction in the normalised transport. This despite the fact that prolonged curing and the use of SCMs in particular SF and GGBS are known to be very effective in densifying microstructure and reducing mass transport. Fig. 5 shows that these measures were not effective in mitigating the effect of spacers (PS or CS). In fact, samples with SF give some of the highest normalised transport coefficients suggesting that spacers negate the beneficial effect of SF.

Another method for analysing the results is to calculate the percentage change in mass transport in samples with spacers compared to the control reference and plot the data as a frequency distribution (Fig. 6). Here data from different ages, binders and transport types are combined. Overall, the change in transport ranges between -35% and +5580%, with the vast majority showing an increase. Samples containing plastic spacers and 50°C drying gave the greatest increase in transport.

It is important to consider the volume of the tested concrete when discussing the effect of spacers on transport. The normalised transport values and the calculated percentages were determined from 100∅ × 50 mm disc samples with centrally placed spacer. The spacer occupies a significant volume of the test sample and therefore the magnitude of change attributed to the spacer is size dependent. For example, the effect of spacers on mass transport reported here would be higher if measurements were made on a smaller test sample, and vice-versa.

3.3 Correlation between porosity and transport

The accessible porosities measured by vacuum saturation are shown in Table 4 and Table 5. Porosity decreased with increasing curing age, as expected. Samples containing SF achieved the lowest porosity, followed by GGBS and FA. Increasing drying severity increases accessible porosity. Fig. 5d shows the normalised porosity of samples containing spacers relative to the control reference. The presence of a spacer increased sample porosity in most cases. However, the magnitude is relatively small compared to the change

in transport coefficient. Fig. 7 shows that the measured transport coefficients are correlated to accessible porosity and connectivity. As expected, samples with higher porosity gave higher transport.

3.4 Fluorescence epoxy penetration depth

Fig. 8 and 9 show fluorescence images of sample cross-sections after epoxy impregnation from the bottom exposed surface. Fig. 10 presents the maximum depth of epoxy impregnation measured with image analysis. The results show that the presence of a spacer increases epoxy penetration, particularly at the spacer interface and within the spacer itself. Plastic spacers caused the largest epoxy penetration. Samples without spacers, particularly those with SF showed the least epoxy intrusion in all cases.

Increasing the severity of drying led to greater epoxy penetration, particularly at the spacer-concrete interface. Some microcracking can be seen near the exposed surface of cementitious spacers. The cementitious spacers are dense (w/b 0.35) relative to the surrounding concrete (w/b 0.4), and the epoxy moved mainly through cracks in the spacer (Fig 8). Samples with plastic spacers dried at 50°C showed penetration across the entire thickness (50 mm), with the majority occurring at the interface and through the concrete nestled within the spacer (Fig. 9).

3.5 Carbonation depth

Table 6 presents the average and maximum carbonation depths for 120-day cured samples after exposure to 3% CO_2 at 30°C 75% RH for 7 months. Results are consistent with the trends observed in the preceding sections. Samples containing SF show no visible signs of carbonation (from phenolphthalein testing) while those containing FA and GGBS have the highest carbonation depths. The presence of a spacer increased carbonation depth in all cases, especially in the case of plastic spacers. Visual inspection found preferential carbonation near the spacer-concrete interface as shown in Fig. 11, implying that the interface is more porous and less resistant to transport. However, the cementitious spacer itself does not appear to be affected by carbonation as much. These observations are consistent with those from epoxy impregnation (Figs. 8 and 9).

3.6 Microstructure of spacer-concrete interface

Fig. 12 presents the porosity gradient from the interface measured using EDM image analysis (Section 2.6). Fig. 13 shows typical BSE images of the spacer-concrete interface microstructure. It can be seen that the average porosity is very high at the interface and decreases to a relatively stable value corresponding to the bulk paste porosity farther away. Accordingly, the unreacted cement content increases from near zero at the interface to the bulk paste value. These features are observed regardless of curing age, binder or spacer type. It is also worth noting that the BSE images taken from the gently-dried samples (21°C, 75% RH). The presence of spacer disturbs the microstructure of the surrounding concrete, and this remains even in well-cured concretes containing SCMs.

The affected region is heterogeneous and spatially variable, with an average width of ~ 40 μm from the interface. Compared to cementitious spacers, plastic spacers produced stronger gradients, in particular a porosity in excess of 80% within the first 10-15 μm from the spacer (Fig. 12). The high interfacial porosity is attributed to bond failure between plastic and concrete, as seen in Fig. 13d. The width of the bond crack increases with age, presumably because the older samples contained more hydration products and therefore additional shrinkage occurred with drying.

Such features are less extreme in samples with cementitious spacers compared to plastic spacers. Overall, the average interfacial porosity is a factor of 3 to 6 higher than the bulk paste farther away. Bond cracking between cementitious spacer and concrete occurred in some locations, but the cracks are shorter and narrower compared to plastic spacers. The cementitious spacer itself contains large amounts of unreacted GGBS and is dense compared to the surrounding concrete (Fig. 13a-c). Therefore transport occurred mainly through the interface and surrounding concrete, rather than through the spacer itself. It is also worth noting that the porosity and unreacted cement content decreased with longer curing. Samples with SF show the lowest detectable porosity, consistent with the data shown in Tables 4 and 5.

4. Discussion

4.1. Influence of SCMs and spacers on transport

It is instructive to compare the data from this study to that of Alzyoud et al. [17] who studied concretes made from 100% CEM I with the same w/b ratio and spacer types, using the same test methodology as the current study. The measured transport coefficient after 28-day curing and conditioning at 20°C, 75% RH ranged from 20×10^{-9} to 32×10^{-9} m^2/s for diffusivity, 57 to 79 $g/m^2min^{0.5}$ for sorptivity and 15×10^{-18} to 57×10^{-18} m^2 for permeability. Comparing these to the data shown in Table 4, it can be seen that blended concretes are denser and have lower transport coefficients. When dried to 50°C, Alzyoud et al. [17] reported the following ranges: 59×10^{-9} to 163×10^{-9} m^2/s for diffusivity, 73 to 106 $g/m^2min^{0.5}$ for sorptivity and 51×10^{-18} to 120×10^{-18} m^2 for permeability. Referring to data in Table 5, it can be deduced that blended concretes have comparable diffusivity and sorptivity after drying at 50°C, but substantially higher permeability than pure CEM I systems.

These observations are consistent with the fact that the use of SCMs alters the type and quantity of hydration products [18]. The SCMs react to generate additional solids, particularly C-S-H. SF is known to have higher pozzolanic reactivity and filling effect compared to FA and GGBS. This leads to greater surface area, pore refinement and de-percolation relative to CEM I systems [43]. However, drying at elevated temperature removes the water within hydrates. The rise in transport may be due to the increased volume and connectivity of accessible pores, microstructural changes induced by dehydration of Aft and AFm phases, partial collapse of C-S-H [50], pore redistribution/coarsening [51-53], and shrinkage microcracking [35, 38, 39, 48, 54-56]. Furthermore, blended systems are more susceptible to shrinkage, and therefore more sensitive to drying, particularly those with SF. The effect of damage induced by drying is more severe for dense systems (SF) and for pressure-induced flow [48].

Alzyoud et al. [17] reported that CEM I concretes with spacers consistently showed higher mass transport compared to controls, by about 10% to 300%. The average increases in diffusivity, permeability and sorptivity attributed to spacers were 57%, 138% and 27% respectively [17]. For blended concretes, the average increases in oxygen diffusivity, oxygen permeability and water sorptivity were 31%, 1210% and 42% respectively. Therefore, the negative effect of spacers is of similar magnitude to CEM I concretes for diffusivity and sorptivity, but substantially higher for permeability. Blended concretes with plastic spacers dried at 50°C performed the worst, increasing permeability by more than a factor of 10× (Figures 5 & 6). Therefore, it seems that the benefits of SCMs can be offset by the presence of spacers in some conditions.

Spacers are either non-porous (plastic) or dense (cementitious spacer) relative to the concrete around it. Furthermore, the spacer occupies a significant volume of the test sample, ~14% for samples with cementitious spacers and ~7% for plastic spacers. Therefore, spacers should behave as barriers to flow. But the results collectively show the opposite, that the inclusion of spacers facilitate transport of gasses, liquids and ions regardless of whether the mechanism is due to a gradient in concentration, pressure, potential or capillary suction. It is also important to emphasise that the magnitude of change in measured transport is expected to exhibit a size effect, i.e. the smaller the test sample compared to that of the spacer, the greater the increase in transport. In other words, the transport through the spacer interface relative to the bulk concrete is a lot higher than the values reported here.

4.2. Microstructure of spacer-concrete interface containing SCMs

Spacers produce microstructural features that are similar to the interfacial transition zone (ITZ) between aggregate and cement paste [23-25] or the interface between reinforcing steel and concrete [57, 58]. The cement deficiency at the interface is due to poor particle packing against larger surfaces, i.e. “wall effect”. The larger interfacial porosity is due to high initial water/cement ratio, micro bleeding and/or entrapment of bleed water on spacers. The microstructure is weak and it is therefore not surprising to observe de-bonding at the spacer-concrete interface. Bond cracking along the interface is induced when differential volumetric changes (thermal expansion, drying or autogenous shrinkage) and relative displacements between spacer and concrete, produce local stress concentrations exceeding its bond strength.

The bond between plastic spacer and concrete is evidently much weaker compared to that for a cementitious spacer. This is presumably due to the smooth non-porous surface of plastic spacers combined with poor thermal compatibility between plastic and cementitious materials. The coefficient of thermal expansion for polyvinyl chloride is ~50 to 200×10^{-6} per °C [59], which is about 10× to 15× higher than that of concrete

[30]. Therefore plastic spacers undergo a greater expansion on heating and contraction on cooling compared to cementitious spacers or the surrounding concrete. This is exacerbated by shrinkage of the concrete (drying or autogenous) which is of the order of several hundreds of μstrain. Blended systems containing SCMs such as SF, GGBS and FA show greater shrinkage [60-62] compared to pure CEM I systems. Therefore, samples containing plastic spacers perform poorly even when they are not subjected to severe drying. Samples dried at high temperatures undergo greater thermal and moisture gradients that induce to more cracking. All these factors explain the microstructural characteristics seen in Figs. 8 to 13.

The imaging and microstructural characterisation show that spacers increase mass transport because preferential flow occurs through the spacer-concrete interface, which is significantly more porous and micro-cracked than the bulk concrete. Preferential transport also takes place through the concrete nestled within the plastic spacer (Fig. 9). This occurred despite the fact that the spacers selected for this study are considered good quality from a leading manufacturer and that a lot of attention was made during sample preparation to ensure good compaction of the concrete around spacers (Section 2.2). This effect is expected to worsen if larger aggregate particles (> 10 mm) are used because of difficulties in ensuring good placement and compaction within the plastic spacer. It is worth noting that coarse aggregate particles > 10 mm are common in practical concretes.

The effect of spacers on transport is clearly more severe than the interfacial transition zone between aggregate and cement paste, despite both having similar microstructural gradients. This is because spacers span the full concrete cover and provide a direct route for the ingress of external agents to the embedded reinforcing steel. In contrast, the porous regions of ITZ are not uniformly exhibited around aggregate particles, but they are discontinuous and separated by dense bulk paste. Indeed, various studies have shown that the overall impact of the aggregate-paste ITZ on mass transport is low [48, 63-66].

4.3. Implications

The thickness and quality of the concrete cover are important factors governing long-term durability of concrete structures since the cover protects embedded steel reinforcement against corrosion. This is well-known in research and practice. However, the importance of spacers is less appreciated and indeed often neglected. This is probably because spacers seem small and inconsequential, but the study shows that such views are incorrect. For many structures, the locations where reinforcing steel are secured by spacers are more likely to be exposed to aggressive agents that increases the risk of premature corrosion or degradation of the surrounding concrete. A typical structure would contain many such vulnerable locations given that a spacer is required at least every meter length of reinforcement according to design standards [6, 7].

However, spacers are an essential component of concrete structures and there are currently no alternative means for supporting reinforcement without suffering from the same issues discussed in this study. There are many types of spacers available in the market, but their quality and properties are not well-regulated. Although codes of practice state that spacers should not have a negative impact on durability [7, 8], it is unclear if this is achievable and there are no requirements for testing to demonstrate performance or compliance. Many projects do not specify spacers in their design, drawings or contract documents. In the absence of guidance from codes of practice, it is not surprising that spacer selection is often done on the basis of cost. Plastic spacers are most widely used due to their lower cost, yet this study shows that they are also the most problematic particularly when exposed to elevated temperatures.

This study shows that the effect of spacers is greatest on pressure-induced flow (permeability). It is worth noting that in many practical situations, permeability is not considered to be a major property influencing degradation mechanisms compared to other transport properties such as diffusion and absorption. However, there are exceptions to this, such as submerged structures subjected to elevated pressure and long-term wetting. Examples include basements, retaining walls, reservoirs, dams, tunnels, pipelines and waste repositories. Permeability is also an important property for structures where water tightness and barrier against leakage are critical serviceability requirements.

Further work is needed to test a wider range of spacer types to establish their impact on long-term performance of concrete structures. Concrete in practice may contain larger coarse aggregate particles (e.g. 16, 20 or 32 mm) compared to the size used in this study (10 mm). We would expect that larger coarse aggregate to induce a greater wall effect and therefore a more detrimental effect of spacers on mass transport. This is worth exploring in future studies. It is also important to carry out tests on field structures or under conditions that mimic real structures (such as wetting/drying, temperature fluctuations, applied loading etc.)

since these factors are likely to aggravate the effect of spacers. There is a real need to improve spacer design and its implementation in structures. A particular challenge will be to improve the bond and microstructure of the spacer-concrete interface.

5. Conclusions

An experimental programme involving 216 test samples (100∅ × 50 mm) was carried out to examine the influence of supplementary cementitious materials (SCMs) on mass transport properties and microstructure of concretes containing reinforcement spacers. Test variables included SCM type (silica fume SF, fly ash FA, ground granulated blast-furnace slag GGBS), spacer type (cementitious, plastic), curing age (3, 28, and 120 days) and drying regime (21°C, 75% RH and 50°C, 7% RH). The main findings are:

a) Spacers increased transport of gases, liquids and ions, regardless of whether the mechanism was due to gradients in concentration, pressure or capillary suction. The extent of increase was dependent on the type of spacer, drying regime and transport mechanism. In contrast, binder type and curing age have little influence. The negative effect of spacers was also detected when samples were gently dried at 21°C, 75% RH.

b) The overall change in transport (diffusivity, permeability, sorptivity) ranged between -35% and +5580%, measured on 100∅ × 50 mm sample with a centrally placed spacer. The vast majority (87%) of samples showed an increase. Samples with plastic spacers and 50°C drying gave the greatest increase in transport, by up to a factor of 57× compared to 16× for cementitious spacers. As expected, permeability was most affected compared to other transport coefficients.

c) Samples containing 8% SF had the lowest porosity, transport properties and carbonation depth, followed by 60% GGBS and 30% FA. When dried to 50°C however, the densest samples experienced the highest percentage increase in transport. Change in transport caused by drying is much larger compared to increasing curing age (3 to 120 days) or varying binder type (SF, FA, GGBS).

d) The negative effect of spacers on blended systems was similar in magnitude to pure CEM I systems for diffusivity and sorptivity, but substantially higher for permeability. Although the use of SCMs and prolonged curing (120 days) improved microstructure and decreased overall transport, these measures did not sufficiently mitigate the effect of spacers. The benefits of SCMs can be negated particularly when plastic spacers are used.

e) Spacers enhanced the depth of carbonation and fluorescent epoxy penetration in all cases, especially for plastic spacers. Visual inspection found preferential transport and carbonation along the interface between spacer and concrete.

f) Microstructural analyses showed that the spacer-concrete interface had greater porosity, less cement, and thus greater w/b ratio relative to the bulk concrete. The size of the affected zone was ~40 μm. The high porosity was due to particle packing effects, bleeding and de-bonding microcracks along the interface. Plastic spacers caused the highest porosity gradients due to poor plastic-concrete bond, compounded by a greater mismatch in terms of thermal expansion/contraction and shrinkage (drying or autogenous) of the surrounding concrete.

g) The negative effect of spacers on mass transport was caused by preferential flow through the porous and micro-cracked spacer-concrete interface. Preferential transport took place through the concrete nestled within plastic spacers. This spanned the concrete cover and exposed embedded reinforcing steel to external aggressive agents, increasing the risk of premature corrosion or degradation of surrounding concrete. This effect is not currently recognised by most researchers or practitioners.

Acknowledgements

F. Muslim gratefully acknowledges the financial support for her PhD study provided by the Indonesian Endowment for Education (LPDP). We thank Hope Construction Materials, Lafarge-Holcim and Elkem for provision of materials. We also thank Mr. Evangelos Pastras, Ms. Xianyi Yu, Mr. Zheng Gu, Mr. Joshua Agbede and Mr. Andrew Morris for their assistance with the laboratory work. The research leading to this publication benefitted from EPSRC funding under grant No. EP/R010161/1 and from support from the

UKCRIC Coordination Node, EPSRC grant number EP/R017727/1, which funds UKCRIC's ongoing coordination.

References

[1] Concrete Society Report CS 101: Spacers for reinforced concrete. Standard provisions for achieving cover encircling reinforcing steel, Crowthorne, 1989, pp. 30.

[2] E.S. King, J.M. Dakin, CIRIA C568: Specifying, detailing and achieving cover to reinforcement, Construction Industry Research and Information Association, London, 2001.

[3] C. Shaw, Cover to reinforcement: getting it right, The Structural Engineer, February (2007) 31-35.

[4] R. Barnes, Concrete Advice No. 43: Spacers and visual concrete, Concrete Society, London, 2012.

[5] CRSI, Placing reinforcing bars: recommended practices, 9th ed., Concrete Reinforcing Steel Institute, Schaumburg, IL, 2011.

[6] BS EN 7973-2: 2001 Spacers and chairs for steel reinforcement and their specification. Part 2: Fixing and application of spacers and chairs and tying of reinforcement, BSI Standards Publication, London, 2001.

[7] BS EN 7973-1: 2001 Spacers and chairs for steel reinforcement and their specification. Part 1: Product performance requirements, BSI Standards Publication, London, 2001.

[8] BS EN 13670: 2010 Execution of concrete structures, BSI Standards Publications, London, 2010.

[9] ACI SP-66 (04): ACI Detailing Manual, American Concrete Institute, 2004.

[10] ACI 315-99 (1999): Details and detailing of concrete reinforcement, American Concrete Institute, 1999, pp. 44.

[11] T. Kawahigashi, K. Kuzume, T. Miyagawa, Deterioration process and estimation of durability of reinforced concrete beams in long-term exposure to marine environment, Proceedings of Japan Society of Civil Engineers, 1999, pp. 71-84.

[12] O.T.K. Vik, The role of bar supports in combating corrosion in reinforced concrete, in: P.H. Brett, N. Banthia, P.J. Buckland (Eds.) The Sixth International Conference on Short and Medium Span Bridges, Canadian Society for Civil Engineering, Vancouver, Canada, 2002.

[13] S. Kenai, R. Bahar, Evaluation and repair of Algiers new airport building, Cement and Concrete Composites, 25 (2003) 633-641.

[14] P. Shaw, A. Materialrontgen, T. Kutti, Field measurement and experience of chloride induced of reinforcement in submerged structures, AB Fardig Betong, Goteborg, Sweden, 2003.

[15] L. Tang, P. Utgenannt, A field study of critical chloride content in reinforced concrete with blended binder, Materials and Corrosion, 60 (2009) 617-622.

[16] M. Geiker, T. Danner, A. Michel, A. Belda Revert, O. Linderoth, K. Hornbostel, 25 years of field exposure of pre-cracked concrete beams; combined impact of spacers and cracks on reinforcement corrosion, Construction and Building Materials, 286 (2021) 122801.

[17] S. Alzyoud, H.S. Wong, N.R. Buenfeld, Influence of reinforcement spacers on mass transport properties and durability of concrete structures, Cement and Concrete Research, 87 (2016) 31-44.

[18] B. Lothenbach, K. Scrivener, R.D. Hooton, Supplementary cementitious materials, Cement and Concrete Research, 41 (2011) 1244-1256.

[19] B.K. Marsh, R.L. Day, D.G. Bonner, Pore structure characteristics affecting the permeability of cement paste containing fly ash, Cement and Concrete Research, 15 (1985) 1027-1038.

[20] S. Li, D.M. Roy, Investigation of relations between porosity, pore structure, and Cl^- diffusion of fly ash and blended cement pastes, Cement and Concrete Research, 16 (1986) 749-759.

[21] R.D. Hooton, Permeability and pore structure of cement pastes containing fly ash, slag, and silica fume, in: G. Frohnsdorff (Ed.), ASTM International, West Conshohocken, PA, 1986, pp. 128-143.

[22] K.E. Hassan, J.G. Cabrera, R.S. Maliehe, The effect of mineral admixtures on the properties of high-performance concrete, Cement and Concrete Composites, 22 (2000) 267-271.

[23] K.L. Scrivener, A.K. Crumbie, P. Laugesen, The interfacial transition zone (ITZ) between cement paste and aggregate in concrete, Interface Science, 12 (2004) 411-421.

[24] J.P. Ollivier, J.C. Maso, B. Bourdette, Interfacial transition zone in concrete, Advanced Cement Based Materials, 2 (1995) 30-38.

[25] J.A. Larbi, Microstructure of the interfacial zone around aggregate particles in concrete, Heron, 38 (1993) 69.

[26] BS EN 197-1:2011 Cement. Composition, specifications and conformity criteria for common cements, BSI Standards Publication, London, 2011.

[27] BS EN 13263-1:2005+A1:2009 Silica fume for concrete. Definitions, requirements and conformity criteria, BSI Standards Publication, London, 2005.

[28] BS EN 450-1:2012 Fly ash for concrete. Definition, specifications and conformity criteria, BSI Standards Publication, London, 2012.

[29] BS EN 15167-1:2006 Ground granulated blast furnace slag for use in concrete, mortar and grout. Definitions, specifications and conformity criteria, BSI Standards Publication, London, 2006.

[30] A.M. Neville, Properties of Concrete, 5th ed., Pearson, Harlow, England, 2011.

[31] BS EN 12620:2002+A1:2008 Aggregates for concrete, BSI Standards Publication, London, 2002.

[32] BS EN 1992-1-1: 2004 Eurocode 2: Design of concrete structures. General rules and rules for buildings, BSI Standards Publication, London, 2004.

[33] BS EN 12390-7 Testing hardened concrete. Density of hardened concrete, BSI Standards Publication, London, 2009.

[34] Z. Wu, H.S. Wong, C. Chen, N.R. Buenfeld, Anomalous water absorption in cement-based materials caused by drying shrinkage induced microcracks, Cement and Concrete Research, 115 (2019) 90-104.

[35] Z. Wu, H.S. Wong, N.R. Buenfeld, Effect of confining pressure and microcracks on mass transport properties of concrete, Advances in Applied Ceramics, 113 (2014) 485-495.

[36] H.S. Wong, N.R. Buenfeld, J. Hill, A.W. Harris, Mass transport properties of mature wasteform grouts, Advances in Cement Research, 19 (2007) 35-46.

[37] L.J. Klinkenberg, The permeability of porous media to liquids and gases, Drilling and production practice, American Petroleum Institute, 1941.

[38] Z. Wu, H.S. Wong, N.R. Buenfeld, Influence of drying-induced microcracking and related size effects on mass transport properties of concrete, Cement and Concrete Research, 68 (2015) 35-48.

[39] Z. Wu, H.S. Wong, N.R. Buenfeld, Transport properties of concrete after drying-wetting regimes to elucidate the effects of moisture content, hysteresis and microcracking, Cement and Concrete Research, 98 (2017) 136-154.

[40] BS EN 14630:2006 Products and systems for the protection and repair of concrete structures. Test methods. Determination of carbonation depth in hardened concrete by the phenolphthalein method, BSI Standards Publication, London, 2006.

[41] H.S. Wong, N.R. Buenfeld, Euclidean Distance Mapping for computing microstructural gradients at interfaces in composite materials, Cement and Concrete Research, 36 (2006) 1091-1097.

[42] M.H.N. Yio, M.J. Mac, H.S. Wong, N.R. Buenfeld, 3D imaging of cement-based materials at submicron resolution by combining laser scanning confocal microscopy with serial sectioning, Journal of Microscopy, 258 (2015) 151-169.

[43] M.H.N. Yio, H.S. Wong, N.R. Buenfeld, 3D pore structure and mass transport properties of blended cementitious materials, Cement and Concrete Research, 117 (2019) 23-37.

[44] J. Schindelin, I. Arganda-Carreras, E. Frise, V. Kaynig, M. Longair, T. Pietzsch, S. Preibisch, C. Rueden, S. Saalfeld, B. Schmid, J.-Y. Tinevez, D.J. White, V. Hartenstein, K. Eliceiri, P. Tomancak, A. Cardona, Fiji: an open-source platform for biological-image analysis, Nature Methods, 9 (2012) 676-682.

[45] C.T. Rueden, J. Schindelin, M.C. Hiner, B.E. DeZonia, A.E. Walter, E.T. Arena, K.W. Eliceiri, ImageJ2: ImageJ for the next generation of scientific image data, BMC Bioinformatics, 18 (2017) 529.

[46] W.-H. Tsai, Moment-preserving thresolding: A new approach, Computer Vision, Graphics, and Image Processing, 29 (1985) 377-393.

[47] H.S. Wong, M.K. Head, N.R. Buenfeld, Pore segmentation of cement-based materials from backscattered electron images, Cement and Concrete Research, 36 (2006) 1083-1090.

[48] H.S. Wong, M. Zobel, N.R. Buenfeld, R.W. Zimmerman, Influence of the interfacial transition zone and microcracking on the diffusivity, permeability and sorptivity of cement-based materials after drying, Magazine of Concrete Research, 61 (2009) 571-589.

[49] S.D. Abyaneh, H.S. Wong, N.R. Buenfeld, Simulating the effect of microcracks on the diffusivity and permeability of concrete using a three-dimensional model, Computational Materials Science, 119 (2016) 130-143.

[50] F. Beltzung, F.H. Wittmann, Role of disjoining pressure in cement based materials, Cement and Concrete Research, 35 (2005) 2364-2370.

[51] L.J. Parrott, W. Hansen, R.L. Berger, Effect of first drying upon the pore structure of hydrated alite paste, Cement and Concrete Research, 10 (1980) 647-655.

[52] I. Maruyama, Y. Nishioka, G. Igarashi, K. Matsui, Microstructural and bulk property changes in hardened cement paste during the first drying process, Cement and Concrete Research, 58 (2014) 20-34.

[53] A.M. Gajewicz, E. Gartner, K. Kang, P.J. McDonald, V. Yermakou, A 1H NMR relaxometry investigation of gel-pore drying shrinkage in cement pastes, Cement and Concrete Research, 86 (2016) 12-19.

[54] J. Bisschop, J.G.M. van Mier, Effect of aggregates on drying shrinkage microcracking in cement-based composites, Materials and Structures, 35 (2002) 453-461.

[55] I. Maruyama, H. Sasano, Strain and crack distribution in concrete during drying, Materials and Structures, 47 (2014) 517-532.

[56] A. Idiart, J. Bisschop, A. Caballero, P. Lura, A numerical and experimental study of aggregate-induced shrinkage cracking in cementitious composites, Cement and Concrete Research, 42 (2012) 272-281.

[57] G.K. Glass, R. Yang, T. Dickhaus, N.R. Buenfeld, Backscattered electron imaging of the steel-concrete interface, Corrosion Science, 43 (2001) 605-610.

[58] A.T. Horne, I.G. Richardson, R.M.D. Brydson, Quantitative analysis of the microstructure of interfaces in steel reinforced concrete, Cement and Concrete Research, 37 (2007) 1613-1623.

[59] S. Patrick, Practical Guide to Polyvinyl Chloride, iSmithers Rapra Publishing2005.

[60] O.M. Jensen, P.F. Hansen, Autogenous relative humidity change in silica fume-modified cement paste, Advances in Cement Research, 7 (1995) 33-38.

[61] S.-i. Igarashi, A. Bentur, K. Kovler, Autogenous shrinkage and induced restraining stresses in high-strength concretes, Cement and Concrete Research, 30 (2000) 1701-1707.

[62] P. Lura, O.M. Jensen, K. van Breugel, Autogenous shrinkage in high-performance cement paste: An evaluation of basic mechanisms, Cement and Concrete Research, 33 (2003) 223-232.

[63] N.R. Buenfeld, E. Okundi, Effect of cement content on transport in concrete, Magazine of Concrete Research, 50 (1998) 339-351.

[64] D. Bentz, E. Garboczi, E. Lagergren, Multi-scale microstructural modeling of concrete diffusivity: Identification of significant varibles, Cement, Concrete and Aggregates, 20 (1998) 129-139.

[65] A. Delagrave, J.P. Bigas, J.P. Ollivier, J. Marchand, M. Pigeon, Influence of the interfacial zone on the chloride diffusivity of mortars, Advanced Cement Based Materials, 5 (1997) 86-92.

582 [66] A. Delagrave, J. Marchand, M. Pigeon, Influence of microstructure on the tritiated water diffusivity of
583 mortars, Advanced Cement Based Materials, 7 (1998) 60-65.

584

Influence of supplementary cementitious materials on microstructure and transport properties of spacer-concrete interface

F. Muslim[1, 2], H.S. Wong[1*], T.H. Choo[1] and N.R. Buenfeld[1]

[1]*Centre for Infrastructure Materials, Imperial College London, SW7 2AZ, UK*

[2]*Civil Engineering Department, Faculty of Engineering, Universitas Indonesia, Kampus UI, Depok 16424, Indonesia*

Table 1. Oxide composition, loss-on-ignition (LOI) and specific gravity (ρ_g) of the binders used.

Binder	Oxide composition (%)									LOI (%)	ρ_g
	CaO	SiO_2	Al_2O_3	Fe_2O_3	MgO	$Na_2O_{(eq)}$	K_2O	SO_3	Cl^-		
CEM I	63.4	20.8	5.4	2.4	1.5	0.3	0.7	2.9	<0.1	2.1	3.15
SF	0.2	98.6	0.3	0.0	0.1	0.2	-	0.1	-	-	2.20
FA	0.1	72.2	24.3	0.4	0.1	0.3	-	0.1	-	-	2.35
GGBS	40.8	36.5	11.6	1.4	7.5	0.5	-	2.1	-	-0.99	2.90

Table 2. Concrete mix proportions.

Mix ID	w/b	CEM I (kg/m^3)	SF (kg/m^3)	FA (kg/m^3)	GGBS (kg/m^3)	Sand (kg/m^3)	Gravel (kg/m^3)
100% CEM I *	0.4	413	-	-	-	726	1090
8% SF	0.4	380	33	-	-	707	1061
30% FA	0.4	289	-	124	-	707	1061
60% GGBS	0.4	165	-	-	248	707	1061

* From mix C10 of Alzyoud et al. (2016)

* Corresponding author. Tel: +44 (0)20 7594 5956.
E-mail: hong.wong@imperial.ac.uk

624 **Table 3. Summary of samples, curing, conditioning and testing regimes.**

Series	Mix	Spacer	Curing (days)	Conditioning	Test
I	100% CEM I * 8% SF 30% FA 60% GGBS	None PS CS	3 28 120	21°C, 75% RH 50°C, 7% RH	Oxygen diffusivity Oxygen permeability Water sorptivity Electrical conductivity
II	8% SF 30% FA 60% GGBS	None PS CS	3	21°C, 75% RH 50°C, 7% RH	Fluorescent epoxy impregnation
III	8% SF 30% FA 60% GGBS	None PS CS	120	21°C, 75% RH	Carbonation
IV	8% SF 30% FA 60% GGBS	None PS CS	3, 120	21°C, 75% RH	Laser scanning confocal microscopy Backscattered electron imaging Image analysis

625 * From mix C10 of Alzyoud et al. (2016)

626

627

628 **Table 4. O_2 diffusivity, O_2 permeability, water sorptivity and accessible porosity measured after**
629 **conditioning at 21°C, 75% RH. Standard errors are shown in brackets.**

Sample ID*	Diffusivity ($\times10^{-9}$ m^2/s)			Permeability ($\times10^{-18}$ m^2)			Sorptivity (g/m^2.min$^{0.5}$)			Porosity (%)		
	3d	28d	120d	3d	28d	120d	3d	28d	120d	3d	28d	120d
8% SF: Co	5.6 (0.42)	3.2 (0.39)	2.4 (0.04)	2.8 (0.40)	1.5 (0.14)	1.1 (0.07)	32.2 (3.46)	7.6 (1.20)	8.3 (0.55)	4.86 (0.11)	2.66 (0.09)	1.58 (0.17)
8% SF: PS	10.8 (0.10)	6.0 (0.46)	2.9 (0.05)	21.1 (2.41)	19.0 (3.80)	6.2 (0.72)	37.2 (2.55)	7.8 (1.07)	6.5 (1.55)	6.27 (0.06)	3.24 (0.07)	2.54 (0.36)
8% SF: CS	25.3 (0.72)	8.5 (0.27)	6.2 (0.06)	46.4 (2.67)	11.3 (1.33)	7.9 (0.08)	48.9 (4.45)	13.9 (1.22)	8.7 (1.95)	7.98 (0.03)	4.96 (0.12)	2.04 (0.10)
30% FA: Co	41.6 (0.86)	12.6 (0.66)	13.4 (0.37)	70.0 (5.56)	9.5 (0.28)	21.6 (0.16)	58.1 (0.16)	19.6 (2.07)	17.4 (1.55)	9.91 (0.22)	7.29 (0.14)	4.94 (0.89)
30% FA: PS	44.3 (1.00)	21.9 (0.59)	15.5 (0.29)	102.2 (8.38)	56.2 (5.84)	30.8 (3.91)	64.1 (1.99)	29.2 (2.27)	23.4 (0.75)	9.98 (0.25)	7.91 (0.15)	5.62 (0.47)
30% FA: CS	47.5 (0.73)	23.3 (0.65)	15.6 (0.67)	94.3 (2.89)	54.2 (1.92)	35.0 (1.00)	62.4 (3.31)	32.5 (1.04)	22.2 (1.40)	9.86 (0.33)	7.02 (0.10)	4.51 (0.18)
60% GGBS: Co	14.0 (1.03)	11.7 (0.59)	11.8 (0.20)	60.0 (1.83)	40.0 (3.06)	9.6 (2.26)	20.1 (3.89)	15.5 (1.15)	15.0 (0.15)	7.99 (0.00)	5.39 (0.14)	3.70 (0.46)
60% GGBS: PS	16.4 (0.90)	14.0 (0.86)	12.2 (0.32)	77.3 (4.30)	70.1 (8.16)	31.1 (1.37)	23.2 (1.53)	17.0 (1.93)	9.7 (1.75)	6.31 (0.11)	7.12 (0.02)	4.20 (0.13)
60% GGBS: CS	17.0 (1.21)	14.5 (1.10)	13.2 (0.73)	85.0 (9.61)	75.0 (5.37)	43.6 (4.35)	26.0 (2.25)	20.0 (0.94)	11.8 (2.30)	8.03 (0.04)	7.16 (0.11)	4.05 (0.11)

630 * Co = control (no spacers), PS = plastic spacer, CS = cementitious spacer

631

632

633

634

635

636

637

638 **Table 5. O_2 diffusivity, O_2 permeability, water sorptivity and accessible porosity measured after**
639 **conditioning at 50°C, 7%RH. Standard errors are shown in brackets.**

Sample ID*	Diffusivity ($\times 10^{-9}$ m^2/s)			Permeability ($\times 10^{-18}$ m^2)			Sorptivity (g/m^2.min$^{0.5}$)			28d porosity (%)
	3d	28d	120d	3d	28d	120d	3d	28d	120d	
8% SF: Co	44.4 (0.76)	46.0 (1.06)	50.6 (0.23)	49.2 (5.30)	50.7 (6.42)	76.4 (2.16)	72.2 (1.70)	49.5 (0.95)	53.7 (-)	9.6 (0.85)
8% SF: PS	46.9 (3.41)	45.4 (0.91)	43.1 (0.41)	2338.6 (231.1)	2463.0 (46.1)	3973.7 (501.4)	136.9 (9.75)	131.5 (14.6)	112.5 (-)	13.5 (1.06)
8% SF: CS	41.1 (0.77)	42.1 (2.49)	49.9 (1.57)	100.6 (19.3)	80.6 (13.4)	447.1 (35.4)	92.2 (5.55)	57.4 (3.25)	63.9 (-)	11.6 (0.92)
30% FA: Co	47.2 (0.63)	39.1 (1.52)	43.9 (0.88)	57.6 (0.66)	44.0 (8.64)	73.2 (5.06)	79.7 (0.95)	65.5 (2.00)	59.2 (-)	13.9 (0.78)
30% FA: PS	45.3 (1.37)	44.4 (1.25)	41.3 (0.79)	2065.2 (274.5)	2499.7 (326.5)	4118.2 (81.8)	149.8 (13.3)	136.7 (16.9)	115.2 (-)	14.1 (0.64)
30% FA: CS	42.5 (0.29)	44.8 (0.79)	40.4 (0.08)	61.9 (0.97)	93.9 (7.19)	368.9 (1.13)	70.5 (0.75)	67.9 (1.50)	72.7 (-)	12.9 (0.78)
60% GGBS: Co	44.1 (0.35)	43.9 (2.32)	46.9 (0.44)	168.8 (45.0)	172.4 (8.03)	162.2 (11.8)	64.0 (0.50)	59.7 (3.10)	49.3 (-)	14.1 (0.92)
60% GGBS: PS	37.1 (0.57)	41.6 (0.93)	42.1 (2.41)	3174.4 (13.0)	2948.8 (183.7)	4231.5 (211.1)	155.8 (17.9)	148.1 (17.2)	101.8 (-)	13.9 (0.57)
60% GGBS: CS	42.5 (1.05)	44.1 (1.65)	43.9 (0.46)	209.8 (64.5)	175.9 (26.6)	696.0 (22.4)	69.9 (5.05)	64.1 (1.30)	57.2 (-)	13.0 (0.71)

640 * Co = control (no spacers), PS = plastic spacer, CS = cementitious spacer

641

642

643 **Table 6. Average and maximum carbonation depth (phenolphthalein) 120d cured samples after**
644 **exposure to 3% CO2 at 30°C, 75% RH for 7 months. Values in brackets are standard errors.**

Sample	Average carbonation depth (mm)			Maximum carbonation depth (mm)		
	Co	PS	CS	Co	PS	CS
8% SF	0	0	0	0	0	0
30% FA	14.9 (0.69)	18.6 (0.59)	17.5 (0.76)	19	20	23
60% GGBS	4.6 (0.54)	11.6 (0.84)	8.1 (0.84)	7	17	14

645 * Co = control (no spacers), PS = plastic spacer, CS = cementitious spacer

646

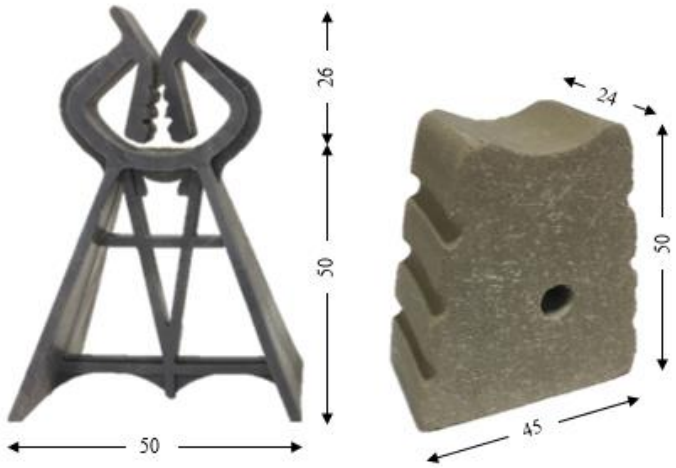

Fig. 1. Single 'A' clip plastic spacer (left) and cementitious spacer (right) for 50 mm cover used in this study. Dimensions are shown in mm.

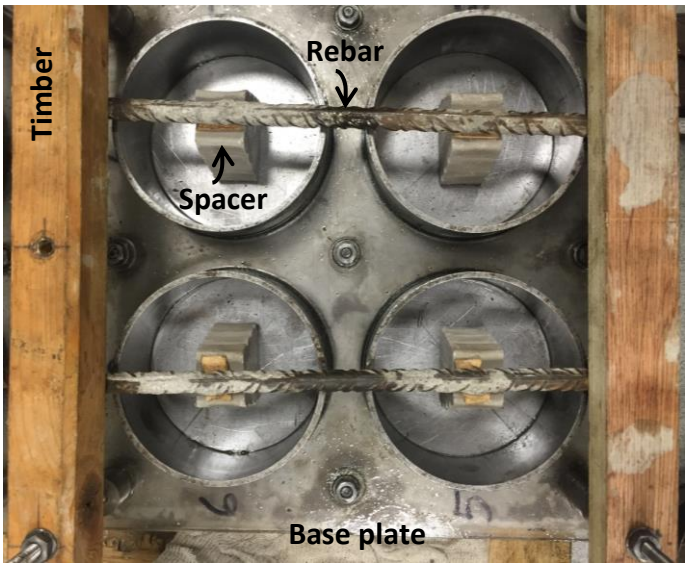

a) Experimental set-up

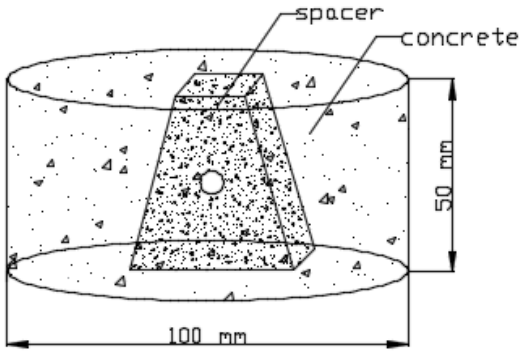

b) Schematic of sample with cast-in spacer

Fig. 2. Setup for preparing cylindrical samples (100∅ × 50 mm) containing reinforcement spacers.

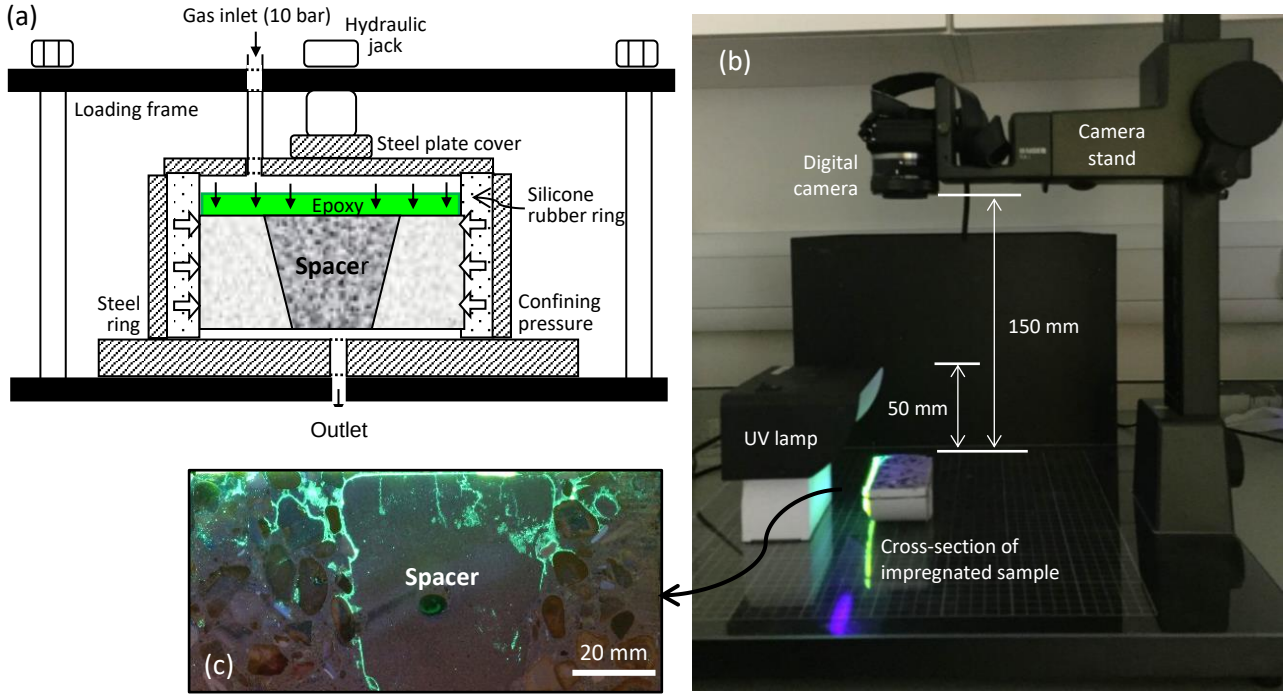

Fig. 3. Setup for a) epoxy impregnation and b) fluorescence imaging. Image (c) shows an example fluorescence image of the impregnated sample.

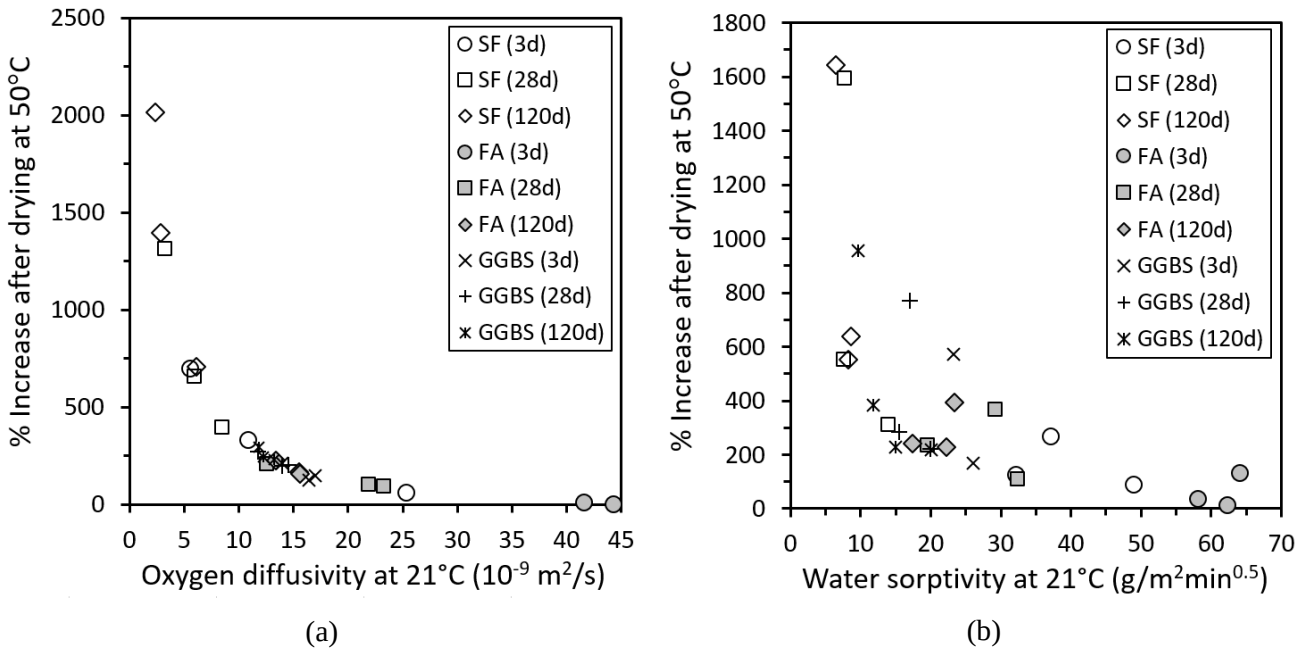

Fig. 4. Effect of drying on mass transport is more pronounced for denser systems.

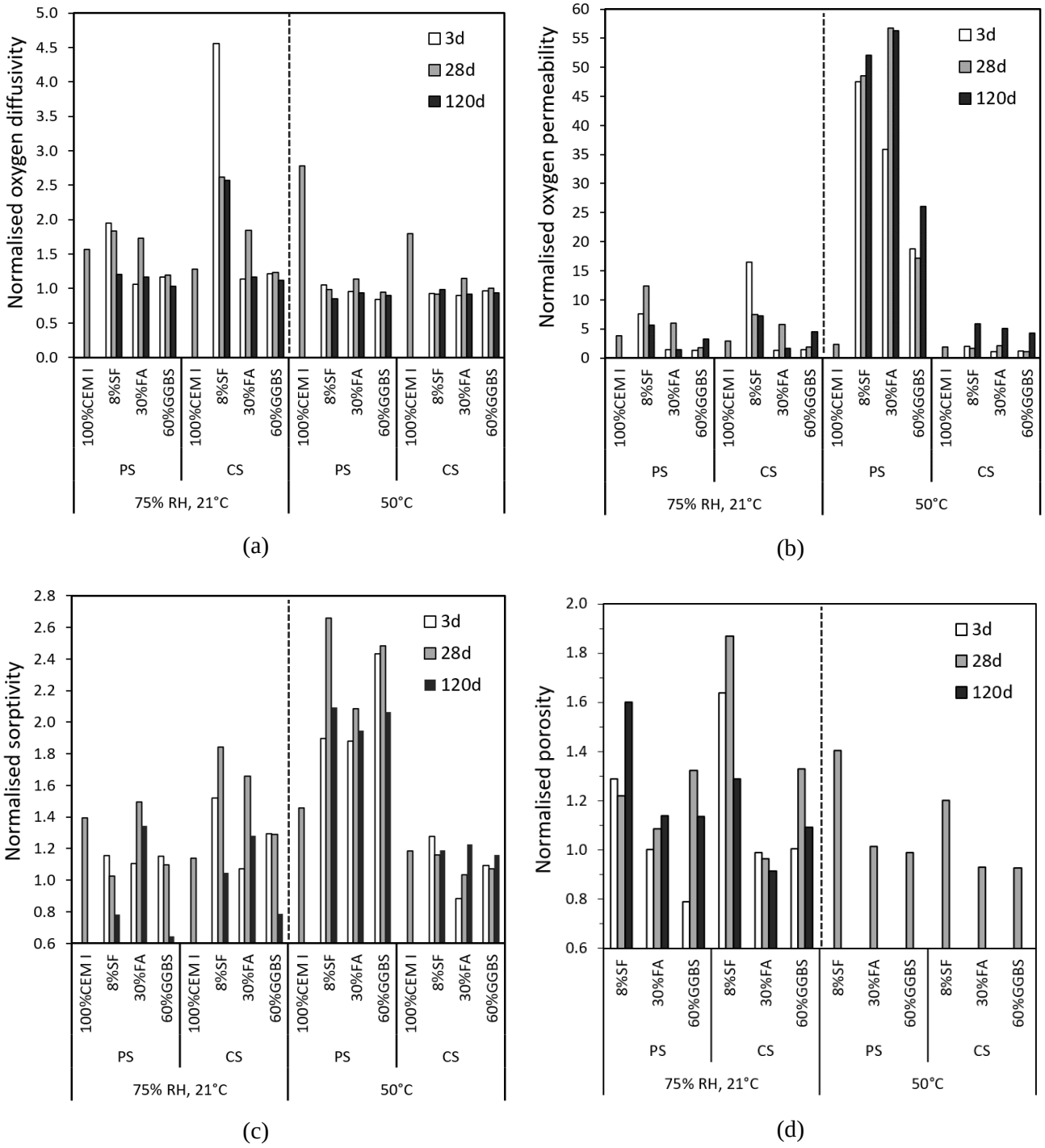

Fig. 5. Effect of spacer type, binder and conditioning on a) O_2 diffusivity, b) O_2 permeability, c) water sorptivity and d) accessible porosity. Data normalised to the respective control reference without spacer (Table 4 and Table 5). PS = plastic spacer, CS = cementitious spacer.

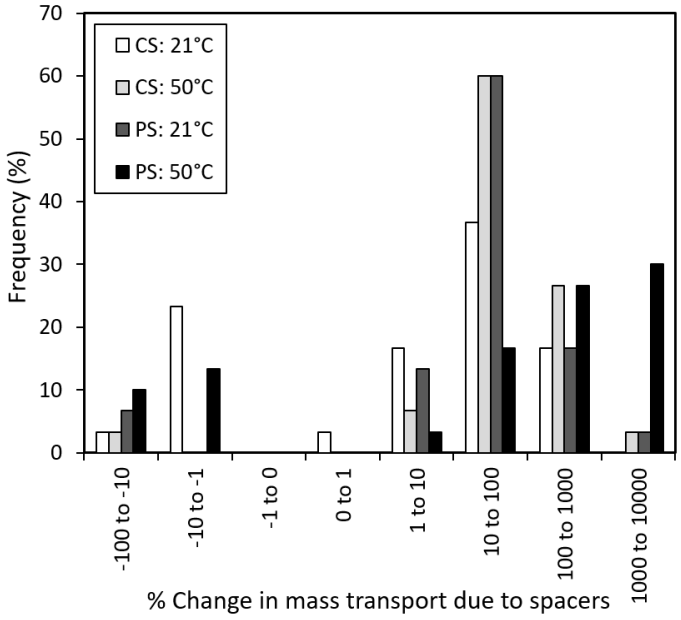

Fig. 6. Frequency histogram of change in mass transport (diffusivity, permeability, sorptivity) due to spacers (n = 120). Note the logarithmic x-axis. Plastic spacers (PS) and drying at 50°C, 7%RH produced the greatest increase in transport.

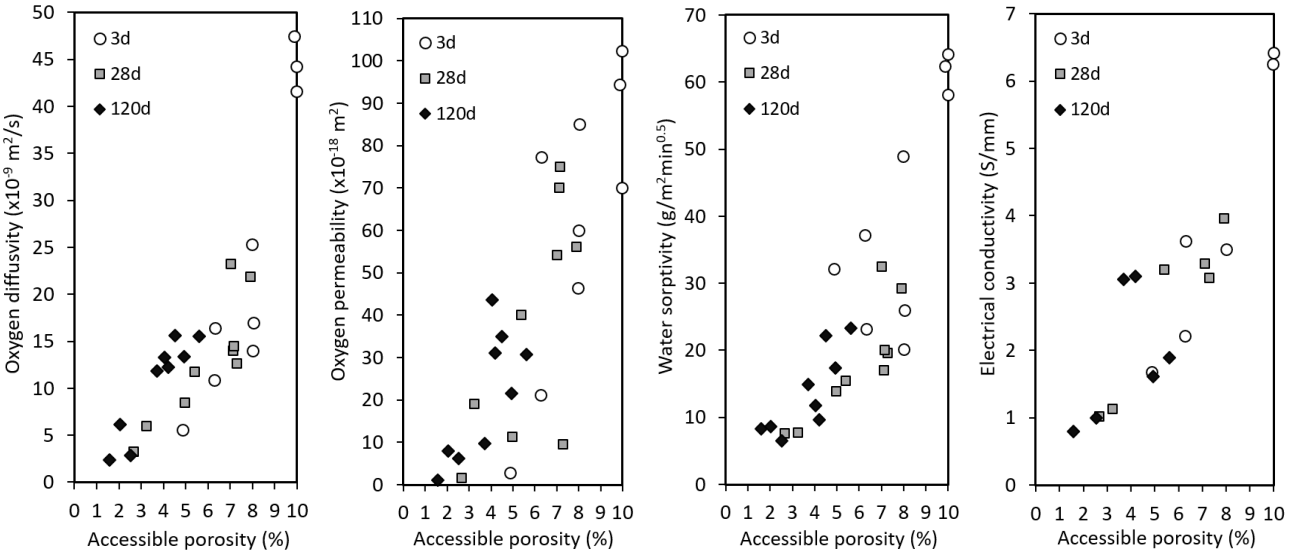

(a) (b) (c) (d)

Fig. 7. Correlation between transport properties and accessible porosity for concrete containing spacers and SCMs

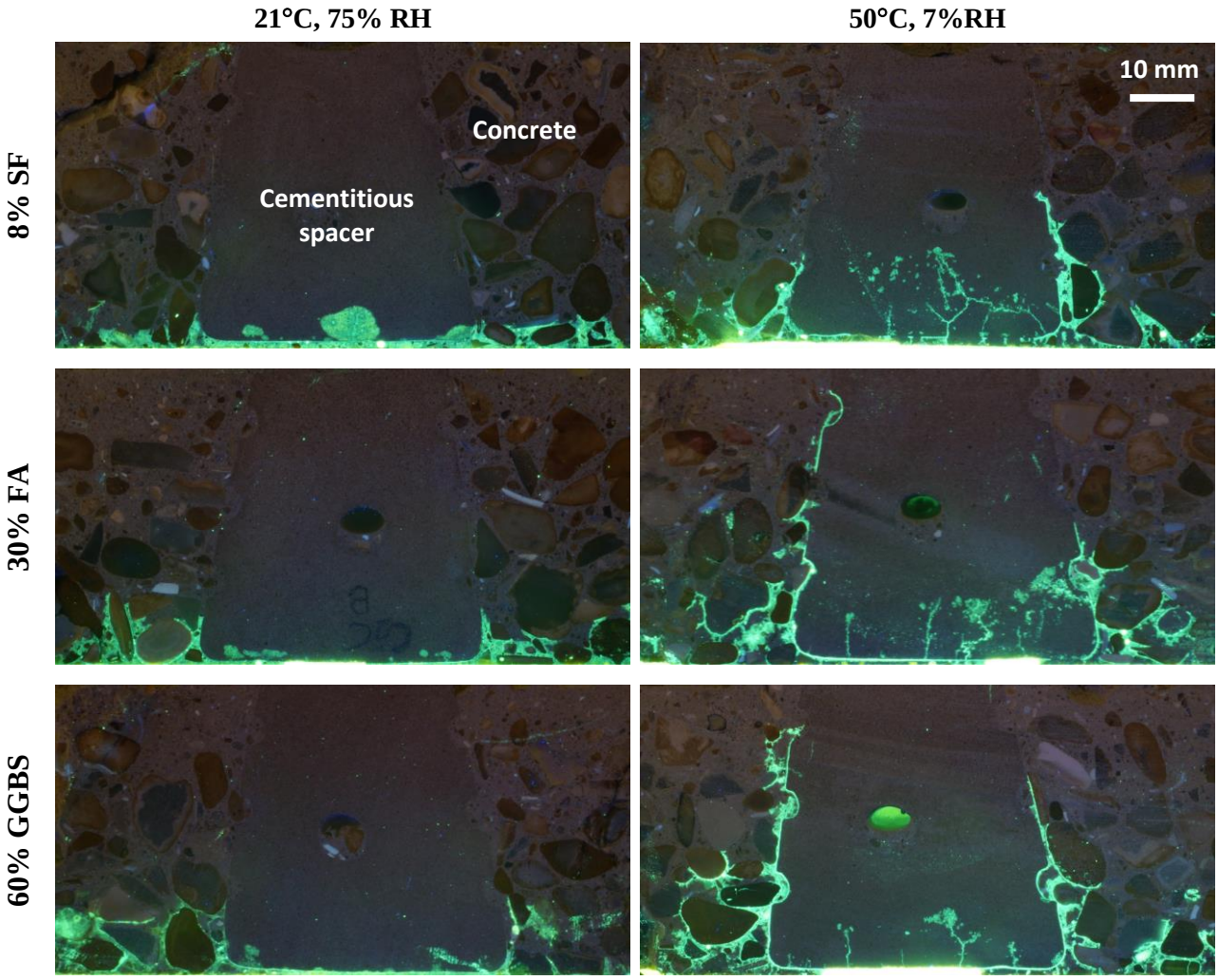

Fig. 8. Fluorescence images show preferential intrusion of epoxy at the spacer-concrete interface after drying at 21°C, 75% RH, and at 50°C, 7%RH. Samples are from Series II containing cementitious spacer.

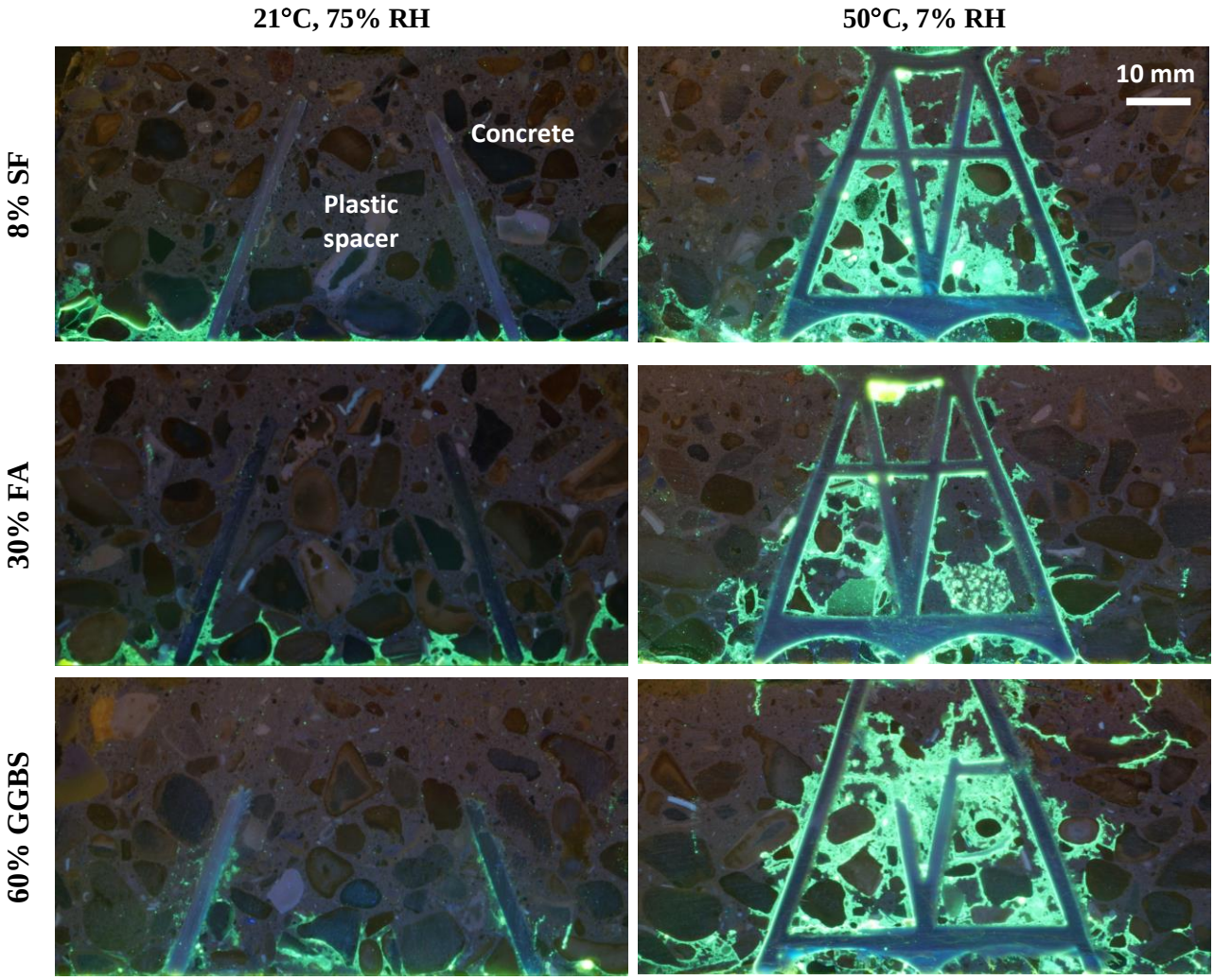

Fig. 9. Fluorescence images show preferential intrusion of epoxy at the spacer-concrete interface after drying at 21°C, 75% RH and at 50°C, 7% RH. Samples contain plastic spacer.

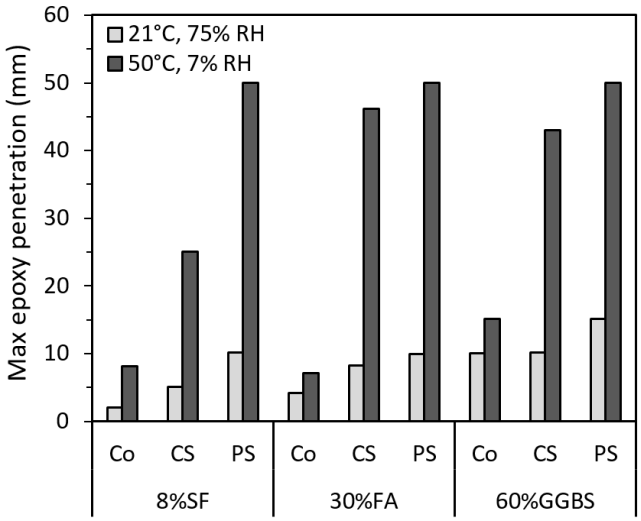

Fig. 10. Effect of spacers, binder type and conditioning regime on the maximum epoxy impregnation.

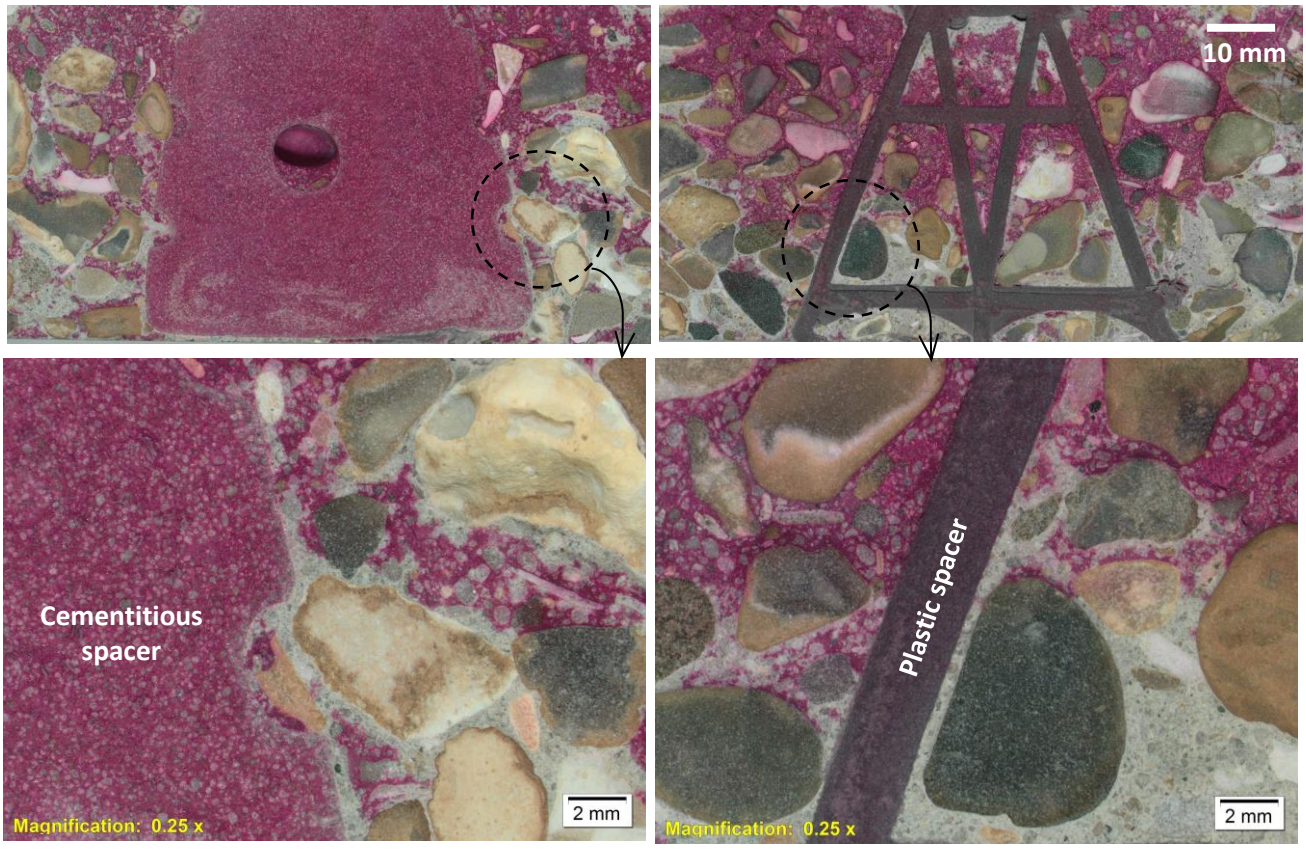

Fig. 11. Cross-section scans after accelerated carbonation in 3% CO2 at 30°C, 75% RH for 7 months. Magnified views show preferential carbonation near the spacer-concrete interface. Sample is 30%FA from Series III.

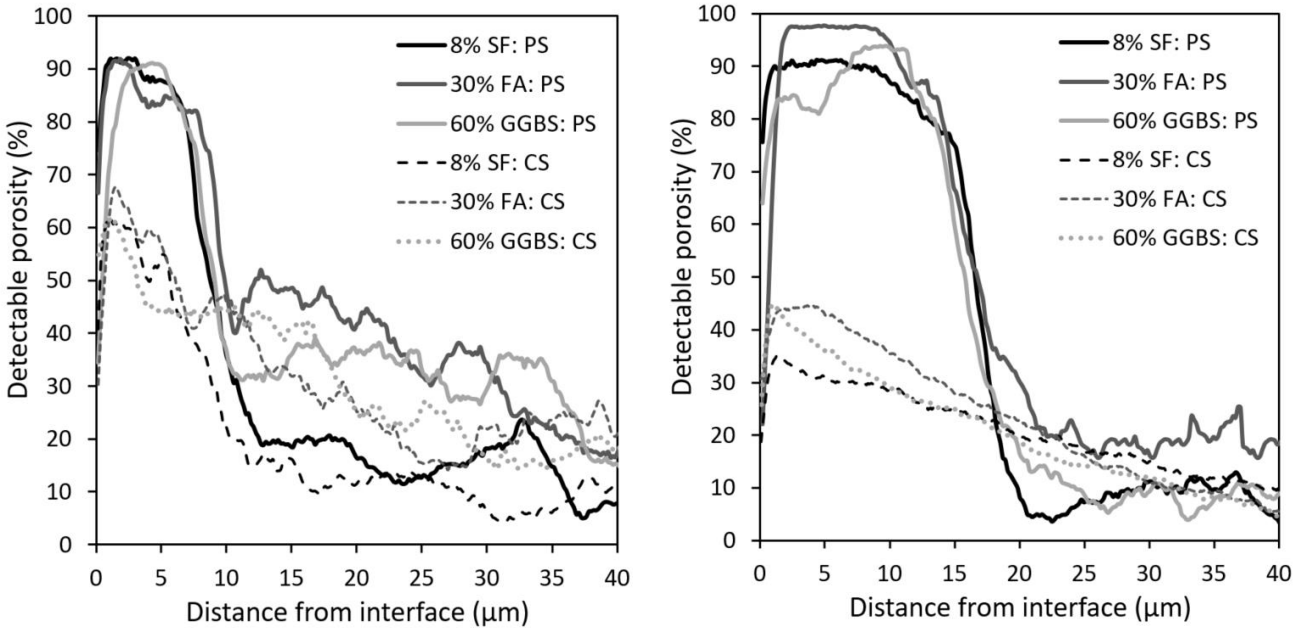

(a) 3-day cured

(b) 120-day cured

Fig. 12. Distribution of detectable porosity from spacer-concrete interface. Samples with plastic spacers (PS) show strong porosity gradients and debonding cracks at the interface.

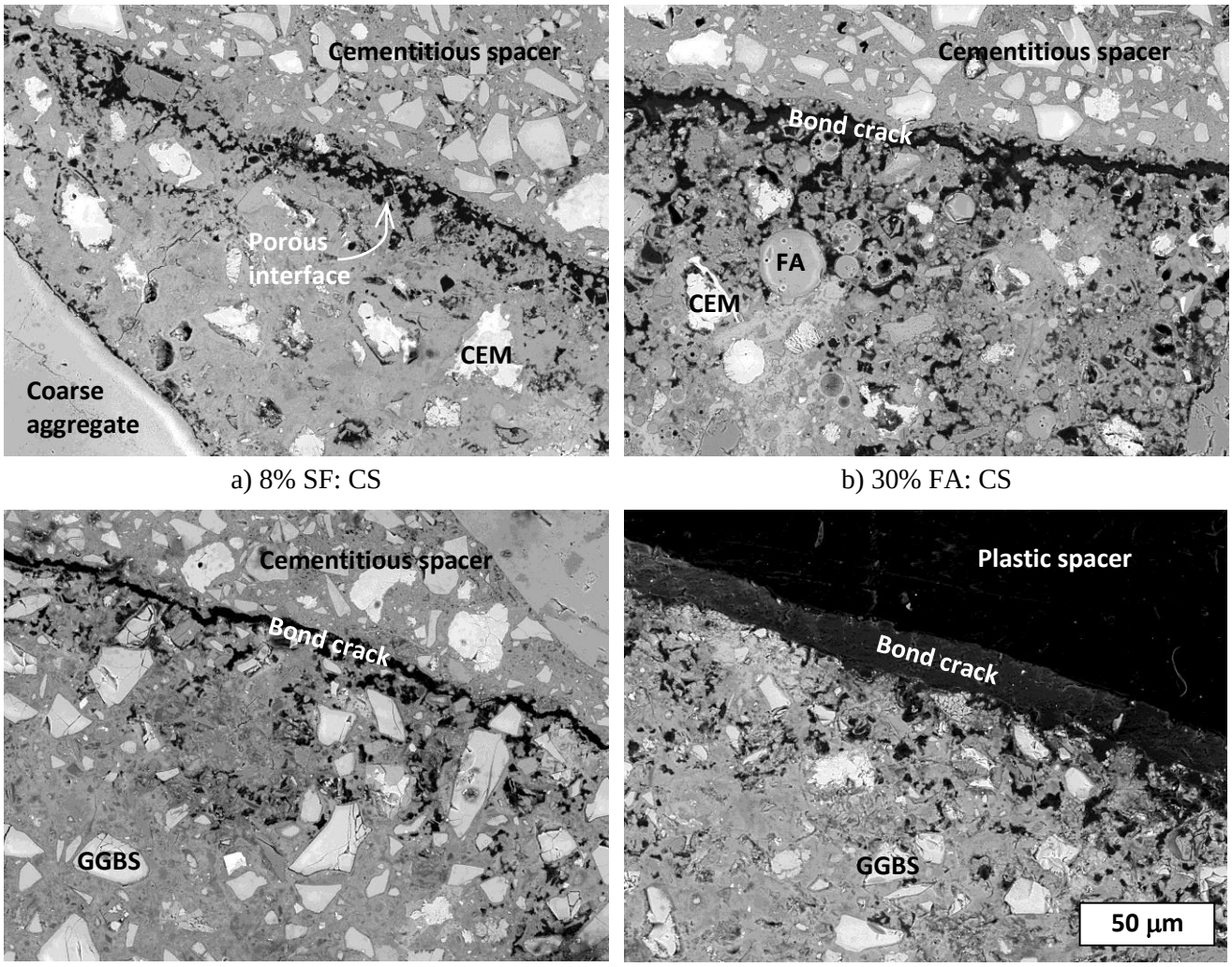

a) 8% SF: CS

b) 30% FA: CS

c) 60% GGBS: CS

d) 60% GGBS: PS

Fig. 13. Example BSE images of spacer-concrete interface that is highly porous and microcracked. Images captured at 500× magnification, field of view 253 × 190 μm.